

On the Influence of Microstructure on the Neutron Irradiation Response of HIPed SA508 Steel for Nuclear Applications

Megan Carter^a, Claudia Gasparrini^{b,c}, James O. Douglas^{a,b}, Nick Riddle^d, Lyndon Edwards^e, Paul A.J. Bagot^a, Christopher D. Hardie^f, Mark R. Wenman^b, Michael P. Moody^a

a - Department of Materials, Parks Road, Oxford, OX1 3PH, UK

b – Department of Materials & Centre for Nuclear Engineering, Imperial College London, London, SW7 2AZ, UK

c - Consorzio RFX, Corso Stati Uniti 4, Padova, 35127, Italy

d – Rolls Royce, PO Box 2000, Raynesway, Derby, DE21 7XX, UK

e – Australian Nuclear Science and Technology Organisation, Lucas Heights, Sydney, NSW 2234, Australia

f – United Kingdom Atomic Energy Authority Materials Research Facility, Culham Centre for Fusion Energy, Culham Science Centre, Abingdon, Oxfordshire, OX14 3DB, UK

First and corresponding author:

Megan Carter

Address: Department of Materials, Parks Road, Oxford, OX1 3PH, UK

Email: megan.carter@materials.ox.ac.uk

Tel: (+44)1865 273777

Keywords: Irradiation hardening; atom probe tomography; nanoindentation; reactor pressure vessel steels; nanoscale clustering

Abstract

The neutron irradiation response of a novel hot isostatically pressed SA508 Grade3 steel was studied, such to deduce any influence this unconventional RPV microstructure has on radiation response. In particular, the role of elevated ferrite fraction was investigated. Neutron irradiation was conducted at $155 \pm 10^\circ\text{C}$ to induce 0.1dpa of damage, this corresponded $2.53 \pm 0.63\text{GPa}$ hardening for the ferrite and $1.94 \pm 0.57\text{GPa}$ for the bainite as measured by nanoindentation. Atom probe tomography detected the presence of Mn-Ni-Si type clusters in both microconstituent phases. The ferrite microstructure showed a greater percentage of solute atoms available to form clusters than bainite, but it also contained a lower cluster volume fraction and number density compared to the bainite.

1. Introduction

Currently one of the most promising nuclear reactor designs is that of the small modular reactor (SMR). By using existing fission technology, the requirement for research is reduced compared to implementing Generation IV type plants, where further proof of concept is needed. The design and construction of SMRs presents the opportunity to utilise novel manufacturing methods to fabricate key aspects of the reactor pressure vessel (RPV), with the aim of enabling longer reactor lifetimes and streamlined installation.

One such innovation is the use of hot isostatic pressing (HIP) to produce certain, appropriately sized, reactor components. This form of powder metallurgy provides greater macroscale and chemical uniformity within manufactured components and net-shape component production (leading to a

reduced need for post-fabrication machining) [1]–[3]. Furthermore, the HIPing process could more easily be implemented as part of an SMR factory assembly line, allowing the rapid, modularised production of the components prior to onsite assembling. However, prior to use in the nuclear industry, the response of HIPed steel to the extreme reactor environment must first be assessed, particularly with respect to the impact of long-term irradiation.

The impact of neutrons on RPV steel has been an area of significant research [4]–[8]. One result of irradiation is the production of nanoscale solute clusters within the RPV steel microstructure under Light Water Reactor (LWR) operating conditions, leading to an increase in yield stress and an increase in hardness. Specifically, the focus of the research community has shifted towards the understanding of the formation, and embrittlement effect, of nanoscale Mn-Ni-Si clusters in nuclear steels [9]–[14]. Of note for this research is the correlation of radiation induced segregation (RIS) and radiation enhanced diffusion (RED) in low-Cu RPV alloys to the segregation of Ni, Mn and Si to solute sinks [14], [15]. Atom probe tomography (APT) has been a critical technique in investigating RIS/RED and the potential mechanisms by which they occur [16], [17].

Compositional variations have been shown to have an impact on the degree of clustering and subsequent hardening, induced in RPV alloys [18]–[21]. Additionally, research into the impact of metallography on irradiation and thermal embrittlement has been shown [22], [23], along with studies on welding effects, such as ferrite nucleation [24] and heat-affected zones [25]. The role of this research is to highlight any differences in irradiation response exhibited by RPV steel produced via HIP that can result in a microstructure that diverges from that typically seen in conventional RPV steels. Generally, RPV steels are forged, resulting in a largely consistent microstructure. Yet, considering the potential for fabrication method diversity associated with SMR designs, there arises the need for supporting investigations concerning the ageing and degradation behaviour of any novel reactor materials [23].

Here, the focus lies on the behaviour of SA508 Grade 3 Class 1 HIP steel, encompassing the influence of HIPed microstructure. Usually, RPV steel microstructures are composed of largely of bainite, through HIP manufacturing process a mixed microstructure consisting of islands of bainite and polygonal ferrite was found [26]. Previous micromechanical testing on the same HIP steel showed that the bainite and ferrite phases had a similar level of hardening when irradiated with He^{2+} ions to 0.6dpa. The nanohardness, measured in continuous stiffness measurement mode, of the unirradiated bainite and ferrite phases, was $2.89 \pm 0.19\text{GPa}$ and $2.69 \pm 0.24\text{GPa}$ respectively, whilst the nanohardness of He^{2+} ion irradiated bainite and ferrite was $6.08 \pm 0.34\text{GPa}$ and $6.03 \pm 0.17\text{GPa}$ respectively [26]. The bainite phase hardened by $3.19 \pm 0.39\text{GPa}$ while the ferrite phase hardened by $3.34 \pm 0.29\text{GPa}$ as it started as the softer phase.

This work therefore aims to study the atomic scale features (especially solute clustering) induced by neutron irradiation of a HIP RPV steel composed of a mixed polygonal ferrite/bainite microstructure with a focus on the differences in the microstructural response of the two phases. This work is also part of a wider collaboration investigating the use of the Open Pool Australian Lightwater reactor (OPAL) at the Australian Nuclear Science and Technology Organisation (ANSTO), to achieve experimental neutron irradiations faster and at lower cost than those provided by alternative test reactors.

2. Experimental Details

Materials and Irradiation Conditions

The HIP steel investigated was of alloy type SA508 Grade 3 Class 1, produced as part of an Electrical Power Research Institute (EPRI) development programme and was provided by Rolls-Royce. It is the same steel investigated by Gasparrini et al. [26]

The resulting alloy composition (of the consolidated material), as determined by chemical analysis methods at Rolls-Royce, is given in Table 1, in addition to the composition of a comparative forged alloy of the same grade used in this project.

Table 1: Nominal composition of HIPed and compared to example SA508 forged sample in at.%, bal Fe.

	<i>Mn</i>	<i>C</i>	<i>Ni</i>	<i>Si</i>	<i>Mo</i>	<i>Cr</i>	<i>Al</i>	<i>Cu</i>	<i>P</i>	<i>S</i>	<i>N</i>	<i>O</i>
<i>HIP</i>	1.252	0.739	0.813	0.415	0.295	0.107	0.039	0.026	0.021	0.010	0.071	0.048
<i>Forged SA508</i>	1.433	0.785	0.775	0.513	0.306	0.235	0.039	0.026	0.007	0.007	0.027	0.003

A result of the HIP process is a steel microstructure different to that produced via conventional forging methods. Sections of the HIP and forged materials were mounted, ground (using Struers® SiC paper grit 600 through to 4000) and polished to 1 micron finish using diamond solution (3µm and 1µm) in combination with Kemet nap cloths, then etched in 2% Nital for 10 seconds. Specifically, it incorporates a relatively high volume fraction of polygonal, idiomorphic ferrite, as shown in Figure 1. ImageJ processing, specifically the morphological segmentation tool from the MorphoLibJ plugin, was used to determine the volume fraction of polygonal ferrite in the HIP sample; approximately 18±2% [27]. For the sake of comparison between this polygonal ferrite and the bainite observed in HIP SA508, from this point polygonal ferrite will be referred to simply as ‘ferrite’. This is with the understanding

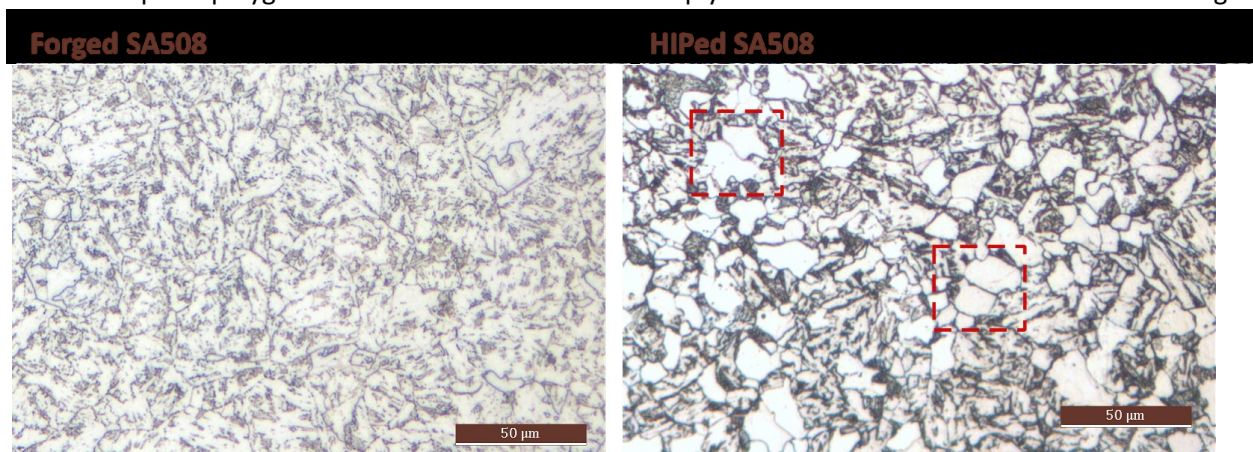


Figure 1: Optical micrographs of forged and HIPed SA508 steel following a 2% nital etch. Ferrite grains within the HIPed microstructure are seen as white and highlighted by the red annotations.

that bainite itself is a mixture of ferrite and cementite, but with a substructure significantly different to that observed in the ‘ferrite’ phase present here [28].

The softness of ferrite compared to bainite is well recognised, and as such metallurgists developing materials for nuclear applications have generally minimised its inclusion within RPV steel microstructures where possible.

Irradiations were conducted in collaboration with ANSTO using the Long Residence Time General Purpose Irradiation Facilities (LRT) at the OPAL multi-purpose research reactor [29]. The OPAL LRTs allow the irradiation of targets contained in sealed irradiation cans. The cans are transferred for irradiation to the rigs within the reflector vessel by means of a pneumatic transport (rabbit) system. The pneumatic transport system is driven by nitrogen gas and the irradiation rigs have provision for cooling of the cans with this flow of nitrogen gas while they are being irradiated. The pneumatic conveyors' loading and unloading are carried out in two shielded hot cells, in which the main operations are automatic. From the pneumatic system shielded hot cells, cans are transferred using an Interbuilding Pneumatic Transfer System (IPTS) to ANSTO's Radioisotope Production and Processing Facility [29].

3mm diameter, 0.1mm thickness samples were produced to a 1200 grit ground surface. Two such discs, each weighing $\approx 4.0\text{mg}$, were irradiated inside a bespoke aluminium irradiation rig, where the discs were placed in slots machined within the solid central aluminium spine of a standard OPAL LRT can. The can was irradiated within the gas-cooled fast flux (FFX-2) facility for 84 days (three OPAL fuel cycles). The can was positioned in a location where it was exposed to a fast neutron flux of $9 \times 10^{12} \text{ ncm}^{-2} \text{ s}^{-1} \pm 10\%$ ($E > 1\text{MeV}$) and a thermal neutron flux of $1.1 \times 10^{14} \text{ ncm}^{-2} \text{ s}^{-1} \pm 15\%$. Overall, this corresponds to approximately $6.5 \times 10^{23} \text{ n/m}^2$ fluence per 3 month irradiation cycle ($E > 1\text{MeV}$). The irradiation temperature estimated by computational fluid dynamics modelling of the gamma heating and gas cooling of the can to be $155 \pm 10^\circ\text{C}$. The location of the FFX-2 irradiation facility and the OPAL pneumatic transfer tubes can be seen in Figure 2.



Figure 2: OPAL Research reactor at power with irradiation facilities and pneumatic transfer tubes illuminated by Cherenkov radiation [29]

Conducting the irradiation at relatively low temperature compared to commercial reactor operation conditions is a restriction imposed by the current OPAL reactor set-up. Although this prevents direct comparison with investigations utilising temperatures typical of pressurised water reactors (PWR), it still allows like-for-like comparisons between the microconstituents being compared in this research.

The potential impact of this lower irradiation temperature is discussed as part of the experimental results.

The damage in dpa experienced from neutron irradiation [4] was estimated using Equation (1):

$$15 \text{ dpa} \approx 10^{22} \text{ n/cm}^2 \quad (\text{for } E > 1\text{MeV}) \quad [1]$$

The steel samples reached a damage level of approximately 0.1dpa after 3, month long, irradiation cycles in OPAL, which corresponds to approximately 25 years of operation in a civil power pressurised water reactor.

Sample Preparation and Ferrite Selection

The 3mm diameter disks were initially ground with Struers® SiC paper grit 800 and 1200 prior to neutron irradiations at ANSTO. After neutron irradiations they were reground and polished at UK Atomic Energy Authority (UKAEA) Materials Research Facility (MRF) using Struers® SiC paper grit 800, 1200, 2000 and 4000, followed by a 3µm and 1µm polishing stage using diamond solution using a Struers MD Nap cloth. A finish suitable for electron backscatter diffraction (EBSD) was achieved using colloidal silica to minimise any surface damaged layer that could mask the irradiation damage.

Unirradiated samples from the as-received alloys were prepared for optical microscopy by grinding with SiC papers of grit 600, 800, 1200 and 4000, followed by a 3µm and 1µm polishing with Kemet nap cloths. The surfaces were then etched in 2% Nital solution for approximately 10s.

A Thermo Scientific™ FEI Helios NanoLab™ DualBeam FIB was used to manufacture specimens for both transmission electron microscopy (TEM) and atom probe microscopy (APT). FIBing of active samples was performed at the UKAEA MRF in the UK. By examining the sample surface for relieved microstructural features using the scanning electron microscope (SEM), the ferrite grains of interest were identified visually. Surface platinum deposition was used to protect the samples from Ga ion damage during the FIB extraction process. An overview of the method used to include both bainite and ferrite within each set of APT samples is shown in Figure 3. For the TEM lamella, after platinum deposition, the thinning was conducted using a Ga ion beam at voltage set to 30 kV and currents of 790pA and 240pA with the lamella tilted by ±1.5°. Some additional steps were taken to minimise FIB induced damage on the sample[30]. Successive polishing stages were conducted at accelerating voltages of 16kV using a current of 150pA with the lamella tilted by ±3°, 5kV using a current of 68pA and 41pA with the lamella tilted by ±5°, and finally 2kV and current of 23pA and 9pA with the lamella tilted by ±7°. The lamella was mounted on a copper grid with platinum. TEM analysis was performed on a JEOL® JEM 2100F™ using a 200keV accelerating voltage and a FEI Talos F200X. Both STEM, coupled with energy dispersive X-ray (EDX) spectroscopy, and TEM, in diffraction mode, were performed to reveal any compositional feature in the samples.

To produce APT samples, individual wedges from three separate lift-out bars, with each bar incorporating a ferrite grain (as shown in Figure 3), were mounted on Si-microposts, following standard lift-out protocols[31]. Tips with an apex of less than 100nm were then produced using annular milling at 30kV 700pA and 80pA, followed by a 2kV polish. As lift-out wedges were mounted onto microposts, its origin within the original cantilever was tracked. This allows approximate knowledge of the microconstituent (ferrite or bainite) comprising each sample. Understanding the differences, if any, in the irradiation response of these two microconstituents is the focus of this investigation. An essential aspect when considering the viability of HIPed components for use in future

reactors is the role of ferrite and any impact it may have on the degree of irradiation embrittlement experienced.

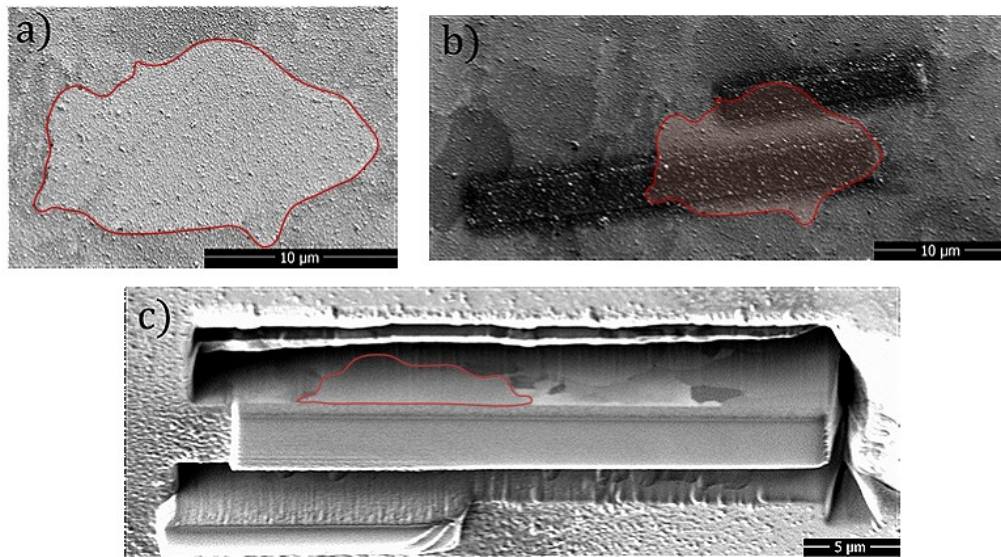


Figure 3: Selection and extraction of ferrite for APT analysis and TEM analyses using FIB-SEM. A ferrite grain (a) is identified, delineated by the red line, which is then incorporated into an atom probe and TEM lift-out bar (b), with the location within the APT bar noted (c).

Nanoindentation and EBSD Mapping

Nanoindentation was used to measure the irradiation induced hardening experienced by the HIP SA508 samples irradiated in the OPAL reactor. Nanoindentation was performed in continuous stiffness measurement (CSM) mode using a frequency set to 45Hz perpendicular to the top surface on as-received and neutron irradiated polished samples. Hardness data were obtained using an Agilent Nanoindenter G200 equipped with a Berkovich tip at UKAEA MRF using a displacement rate of 0.5s^{-1} and Poisson's ratio of 0.3. A total of 80 indents in a 10×8 array were made in the unirradiated and neutron irradiated samples. Indents were positioned 40μm apart and tests were performed in displacement control to a depth of approximately 2μm. Surface approach velocity and harmonic displacement were 10nms^{-1} and 4nm respectively.

To characterise the relative hardness difference between the ferritic and bainitic phases, Electron Backscatter Diffraction (EBSD) maps were acquired on the nanoindented region. EBSD was performed using a TESCAN Mira3 XMH SEM at MRF with an Oxford Instrument Nordlys EBSD detector. The sample was tilted to 70° and the EBSD pattern acquisition was acquired at a voltage of 20kV. Step size of 230nm and exposure time of 18ms were used to analyse sample surface post indentation. EBSD patterns were plotted and analysed using Channel 5™ software with modules Tango™ (mapping) and Mambo™ (pole figure) from Oxford Instruments® HKL™.

Individual indents were attributed as ferrite or bainite measurements based on the location of each indent within the EBSD map. Figure 4 shows the surface of the unirradiated and neutron irradiated samples after nanohardness testing. Due to the manual procedure of the polishing stage on the activated sample, some scratches remained on the surface. The indents that were positioned across

scratches were removed from hardness analysis. EBSD images showing band contours and 10 degrees and 2 degrees grain boundaries (highlighted in post-acquisition analysis), seen in Figure 4, were used to differentiate between the two microconstituents. This was a useful method of distinction due to bainite containing a high level of local misorientation, highlighted by a high density of small angle grain boundaries. As determined by eye, bainite or ferrite-allocated indents were only considered for analysis where the determined grain type contributed the majority of the surface area incident by that indent. In the case of ferrite grains, where the grain size is roughly equivalent to the indenter tip, this corresponded to an indent either hitting the entirety of one grain, or an area where multiple ferrite grains lay adjacent. When indents fell in both microstructures they were labelled as “bainite + ferrite”. Due to the relative sizes of the indents and ferrite grains, alongside the unknown depth of the ferrite into the indenting surface, it is difficult to be confident that each indent designated as within ferrite fell solely within a ferrite grain. One option to mitigate this risk would be to use shallower indentation depths, however, this reduced depth results in increased indentation size effect giving a larger spread in hardness. It was decided to consider hardness values for depths between 100nm and 200nm to reduce the hardness response from neighbour grains.

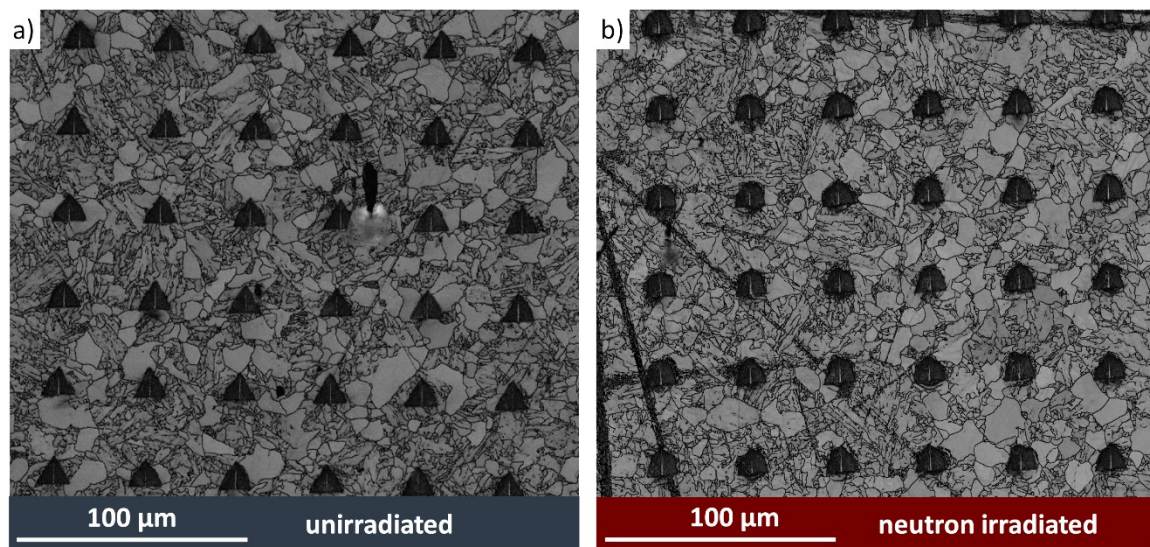


Figure 4: EBSD images after nanoindentation showing band contrast and grain boundaries (10 degrees and 2 degrees) of: a) unirradiated; b) 3 months neutron irradiated HIP SA508 grade 3 steel.

Atom Probe Characterisation of MnNiSi Clusters

APT analysis was performed using the Cameca 5000XR local electrode atom probe (LEAP) at the University of Oxford. Each sample was analysed using voltage pulsing at a specimen temperature of 45K, pulse fraction of 20%, pulse frequency of 200kHz and detection rate of 0.3%. Atom map reconstruction was performed using IVAS software, where any suspected residual Ga-damage was removed from the analysis.

IVAS 3.8.4 core-linkage cluster analysis, derived from the maximum separation method (MSM), was utilised to extract the cluster size (number of atoms), composition and number from each dataset [32]. The key MSM parameters were user determined, in line with previous reports on the use of this algorithm [33]–[37]. A complementary simulated dataset, in which the chemical identities of all the atoms have been randomly swapped to remove chemical-spatial correlations, was generated such to help accurately determine the amount of real clusters for a chosen d_{max} and N_{min} pairing [38]. d_{max} defines the maximum distance that can separate two atoms for them to be determined to belong to

the same cluster. N_{min} is a minimum cluster size used to prevent atoms randomly within d_{max} separation from being included in cluster counts. For each dataset the finalised MSM parameters were chosen such that the number of clusters identified from the random comparator system was less than 5% of the total number of solute clusters identified in the real data. The d_{max} values were 0.45-0.55nm, with an N_{min} between 15 and 20 atoms. The envelope (L) and erosion (E) parameters used in each case were equal to half of the selected d_{max} . The ions included as solute within the MSM calculations were Ni, Si, Mn and P, based on them exhibiting segregation behaviour as shown in the IVAS frequency distribution tool (due to being a low-Cu steel, there was no evidence of Cu segregation). For clarity, given detailed findings on the inclusion on Fe within cluster compositions discussed in [39], [40], Fe was not included in reported cluster compositions. The 29Da peak was set as Ni for all cluster identification and analysis.

An R-script was then applied to extract the volume fraction (f) - based on dividing the number of solute atoms within clusters by the total number of atoms present - of the clusters [14]. Volume fraction is equal to the number of atoms within all identified clusters as a percentage of the total number of identified atoms within the APT dataset, with the method of calculation described in more detail in the Appendix of [14].

Results and Discussion

The steel mixed microstructure characterised by nanoindentation showed that the average hardness of the unirradiated bainite was 3.64 ± 0.46 GPa and that of ferrite was 3.19 ± 0.47 GPa highlighting the softer nature of ferrite. Hardness values were measured in the displacement interval 100-200nm and errors are the standard deviation. Indents that lied across both unirradiated bainitic and ferritic grains showed an intermediate hardness of 3.48 ± 0.44 GPa. The hardness of indents that hit both ferrite and bainite grains in the unirradiated sample was always an intermediate value compared to the hardness of only bainite and only ferrite grains. The error bars, which represent the hardness distribution, are quite large due to the shallow depth, but this depth was chosen to better analyse the hardness response of the single microstructure seen on the surface, in an attempt to minimise the effect of neighbouring grains. Figure 5c shows that, at a depth of approximately 1 micron, the hardness of the unirradiated bainite and ferrite can be distinguished better since the error bars do not overlap. All error bars shown are given as ± 1 standard deviation, and are generally large as a result of the local variations in microstructure between indents. It is the mean values obtained which indicate a small difference between the hardness of ferrite and bainite.

Neutron irradiation induced a considerable hardening in the steel, as shown in Figure 5 a) and b). As can be observed from Figure 5b, a similar hardness was reached by bainite and ferrite microstructures irradiated by neutrons. The hardness of the neutron irradiated bainite was 5.58 ± 0.35 GPa, the hardness of the neutron irradiated ferrite was 5.71 ± 0.43 GPa, while the hardness of indents that lay on both bainite and ferrite grains was 5.42 ± 0.46 GPa. The hardening of the bainite and ferrite grains due to irradiation with depth is shown in Figure 5c: this shows the average hardness for indents that hit only ferritic or bainitic grains. The change in hardness with neutron irradiation is shown in Figure 5d. The larger hardening observed for the ferrite phase can be explained by the fact that it was softer before irradiation than the bainite. The similar hardness response obtained from the two microstructures may be related to the fact that hardening is more influenced by irradiation induced defects than microstructural features.

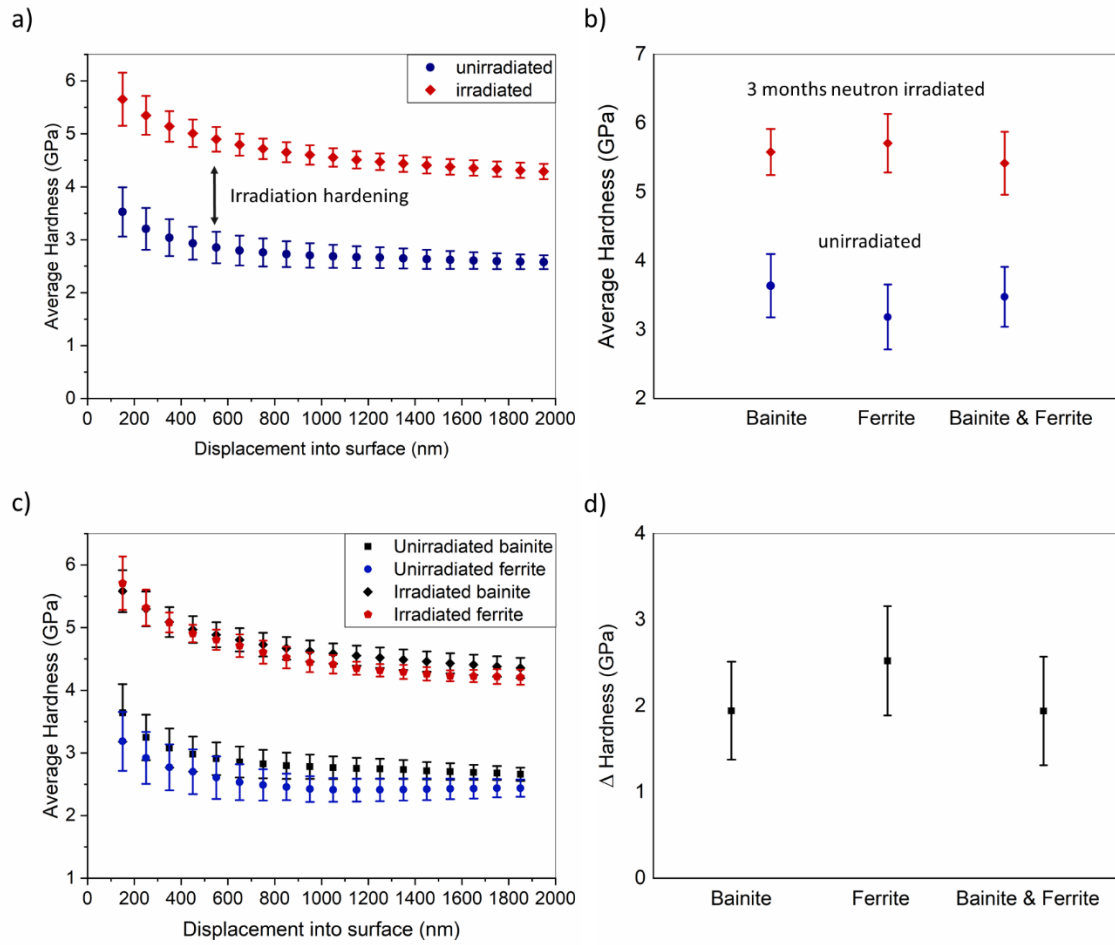


Figure 5: Nanohardness data acquired in CSM mode on unirradiated and 3 months neutron irradiated samples: a) average hardness versus indenter displacement into surface; b) average hardness (sampled at 100 – 200nm displacement) of indents that hit only bainitic, ferritic or both microstructures; c) average hardness of bainitic and ferritic indented grains with depth from the unirradiated and neutron irradiated samples; d) average irradiation hardening, ΔH , due to neutron irradiation for bainitic, ferritic and mixed bainitic/ferritic grains (sampled at 100 – 200nm displacement)

STEM-EDX characterisation of bainite and ferrite samples showed the presence of particles (measuring approximately 30-100nm in size) mainly consisting of aluminium oxide and manganese – silicon nitride particles often nucleated next to molybdenum carbide particles in both unirradiated and irradiated samples. The oxide/nitride particles are considered to be induced by the HIP manufacturing process since higher oxygen/nitrogen content was measured on the steel produced via this route compared to the forged steel (see chemical analyses in Table 1). Some secondary phases enriched in manganese were found in the ferrite phase.

Characterisation conducted by TEM in bright field mode (BF) on unirradiated and irradiated samples did not show any visible irradiation induced damage features: black dots visible on the surface were later identified as surface oxides (Fe_3O_4) by centred dark field (CDF) imaging and selected area diffraction patterns (SADPs) as shown in **Figure 6**. Analysing unirradiated and neutron irradiated bainite grains by HRTEM imaging, only d spacing that were related to ferrite and magnetite, Fe_3O_4 , could be identified. Specifically, 2.017\AA and 2.02\AA d spacings were calculated which were related to the ferrite phase ($a=b=c=2.8664\text{\AA}$ where the $(1\ 1\ 0)$ is 2.027\AA), and d spacings of 2.502\AA , 2.409\AA and 1.713\AA were related to magnetite phase ($a=b=c=8.3960\text{\AA}$ where the $(3\ 1\ 1)$ is 2.5320\AA , the $(2\ 2\ 2)$ is 2.4243\AA and $(4\ 2\ 2)$ is 1.7146\AA).

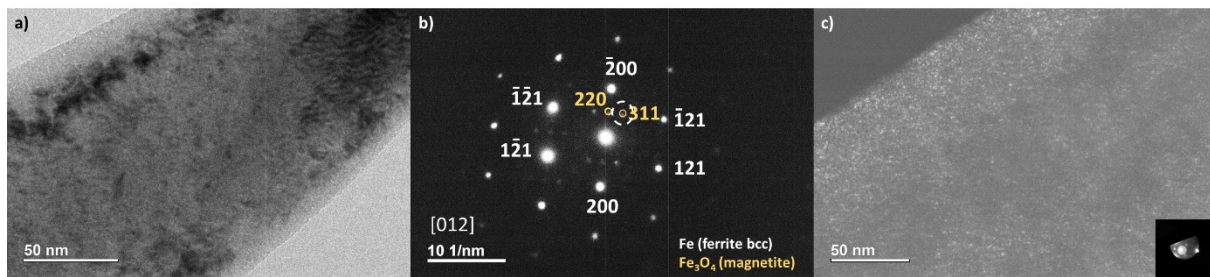


Figure 6 TEM analysis of a ferrite grain from neutron irradiated sample: a) BF TEM analysis, b) SADP (20 cm camera lens) showing the presence of the ferrite matrix and magnetite oxide, the dashed circle highlights the spot chosen for CDF imaging, c) CDF image obtained after 15 seconds exposure, spot chosen is highlighted as dashed white circle in b) and shown in c)

STEM-EDX analysis performed using a higher sensitivity Super-X EDX detector meant it was possible to visualise an uneven distribution of the solutes in the neutron irradiated sample. The presence of 4 single silicon drift detectors enabled the acquisition of more counts in a short time minimising the effect of any sample drift, crucial in this analysis since the clusters are of nanometre scale. Specifically, the distribution of Ni and Mn overlapped when these elements were plotted together (see Figure 7).

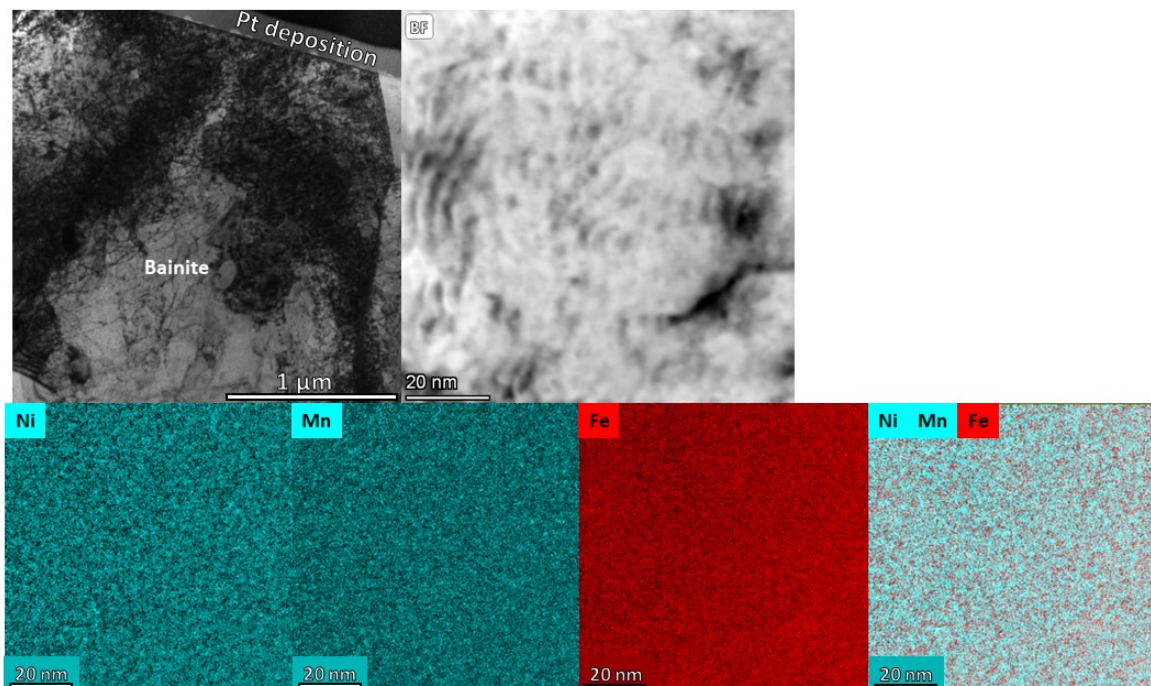


Figure 7 STEM-EDX analysis of a bainite grain extracted from neutron irradiated sample: BF TEM images (top) and STEM-EDX maps of the region shown at high magnification of Ni, Mn, Fe and all three elements together.

The uneven distribution of the solute shown in Figure 7 for Mn, Ni and Fe is, however, subtle and no undisputable evidence of cluster formation can be derived.

Evidence of neutron irradiation clustering was provided by APT analysis on the same samples. Representative atom maps produced by site-specific APT samples taken from ferrite and bainite regions are shown in Figure 8. For visual clarity, all ions except those determined to be involved in clustering have been removed. All clusters are of the Mn-Ni-Si type. Visually, the distribution **and nature of** clusters in bainite and ferrite appear similar. This apparent uniformity in cluster distribution

for bainite and ferrite is supported in further analysis based on cluster composition and volume fraction. The method for calculating cluster volume fraction is described in the Appendix of [14].

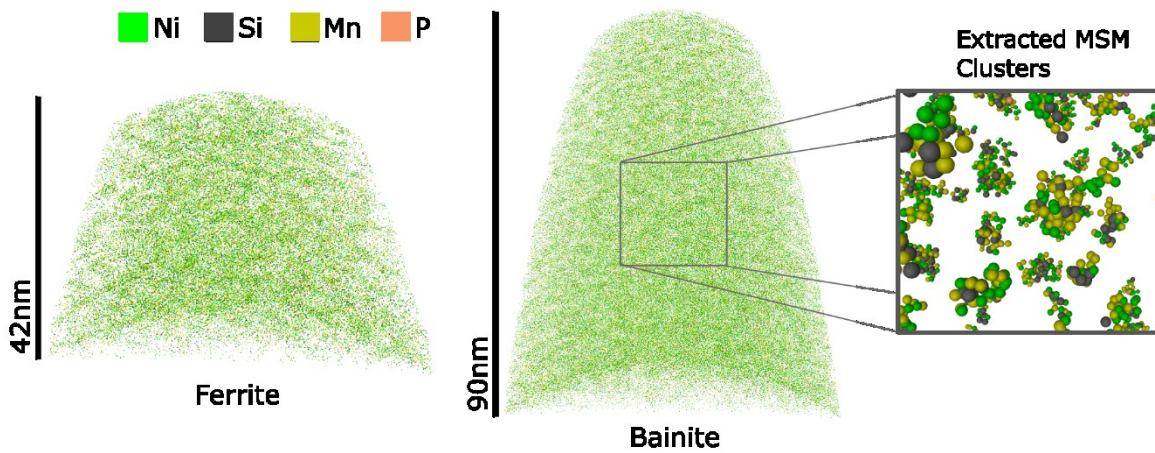


Figure 8: Representative APT atom maps indicating the presence of fine-scale neutron irradiation induced solute clusters in SA508 RPV steel ferrite and bainite samples, following neutron irradiation to 100mdpa at 155°C. An example of the clusters extracted using the Maximum Separation Method is included for the bainite sample, with only the solute atoms shown (for clarity).

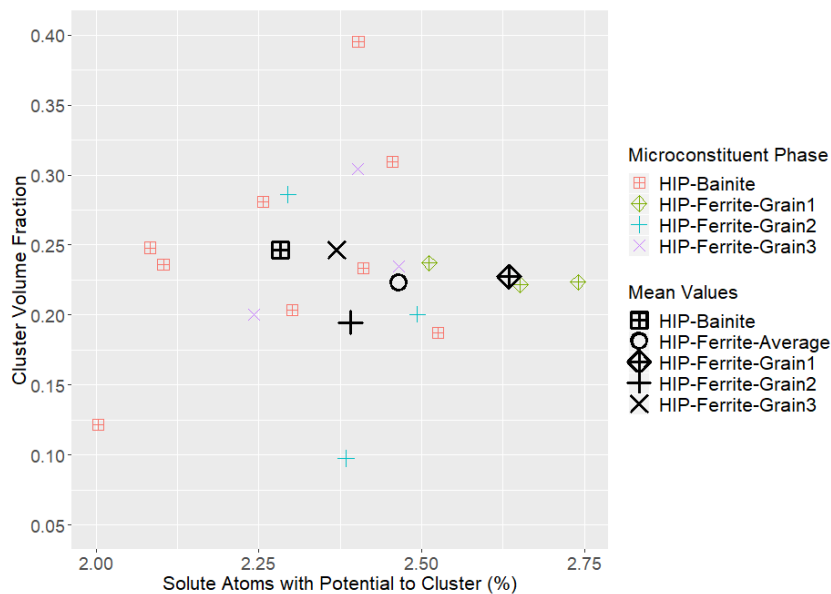


Figure 9: Plot detailing the volume fraction (%) of clusters vs the total number of solute atoms involved in clustering present for each atom probe dataset. The mean values for ferrite and bainite region reconstructions are shown.

Figure 9 compares cluster volume fraction of samples measured from within the bainite and ferrite phases, respectively, against the overall amount of solute atoms (Mn, Ni, Si, P, Cu) contained within each reconstruction. The mean volume fractions are shown in Table 2. There appears to be only limited variation between the microconstituents with respect to average cluster volume fraction. A greater spread of measured cluster volume fraction levels is seen within the baintic reconstructions.

However, this spread in clustering does not seem to affect hardness spread – assuming there exists some form of correlative effect between the number of clusters and the observed hardness since the clusters were observed within very small areas, therefore giving large variance, whilst hardness tests are taken over a larger area and therefore any small area deviations are absorbed.

Evidence of a small difference in cluster volume fraction variance within bainite and ferrite samples may be a result of the more defected microstructure of bainite, leading to a greater spread in the number of defects present in the sampled bainitic regions. Radiation induced segregation is known to involve the diffusion of solute atoms to defects [16], [17], [41]–[44]; although, usually the majority of these heterogeneous nucleation sites are assumed to be solute-defect cluster complexes and stable matrix damage features induced by neutron displacement cascades [45]. The results presented here suggest that pre-existing defects associated with the initial, non-irradiated microstructure (such as dislocations) may increase the likelihood of early-stage heterogeneous cluster nucleation.

Table 2: Average cluster volume fraction and number density for bainite and ferrite APT samples, given to 3 significant figures (3sf).

	Average Cluster Volume Fraction (%) (3sf)	Average Cluster Number Density (m^{-3}) (3sf)
Bainite	0.246 ± 0.073	$4.07 \times 10^{24} \pm 1.46 \times 10^{24}$
Ferrite	0.223 ± 0.055	$3.73 \times 10^{24} \pm 1.04 \times 10^{24}$

The ferrite grains, on average, appear to have a greater amount of clusterable solute, i.e. solute atoms of elements that are actively associated with irradiation-induced cluster formation, within the samples analysed, although it is acknowledged that the spread in data does give overlap in these cluster count distributions. Perhaps counterintuitively, this does not correspond with a higher cluster volume fraction or number density in the ferrite. This suggests that, in comparison to the bainite grains, there is a relative lack of potential nucleation sites within the ferrite matrix, where the cluster number density is limited by number of available point defects (due to both neutron damage and pre-irradiation microstructure).

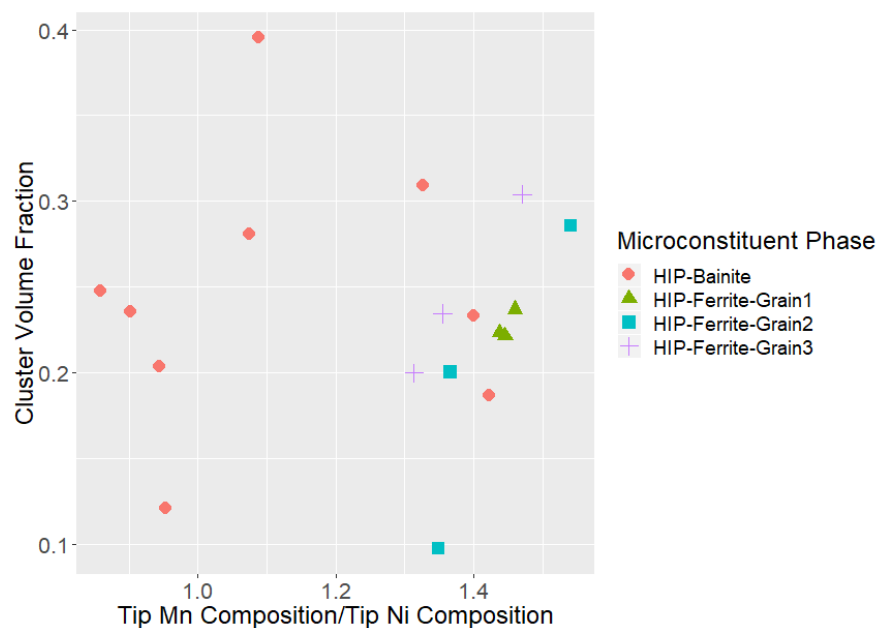


Figure 10: Plot indicating the relationship between the cluster volume fraction observed in samples and the relative Mn content, with respect to Ni.

Whilst all solute elements were investigated to identify concentration fluctuation between tips, only Mn displayed any significant variation. Subsequently, the generally lower clustering-solute content in

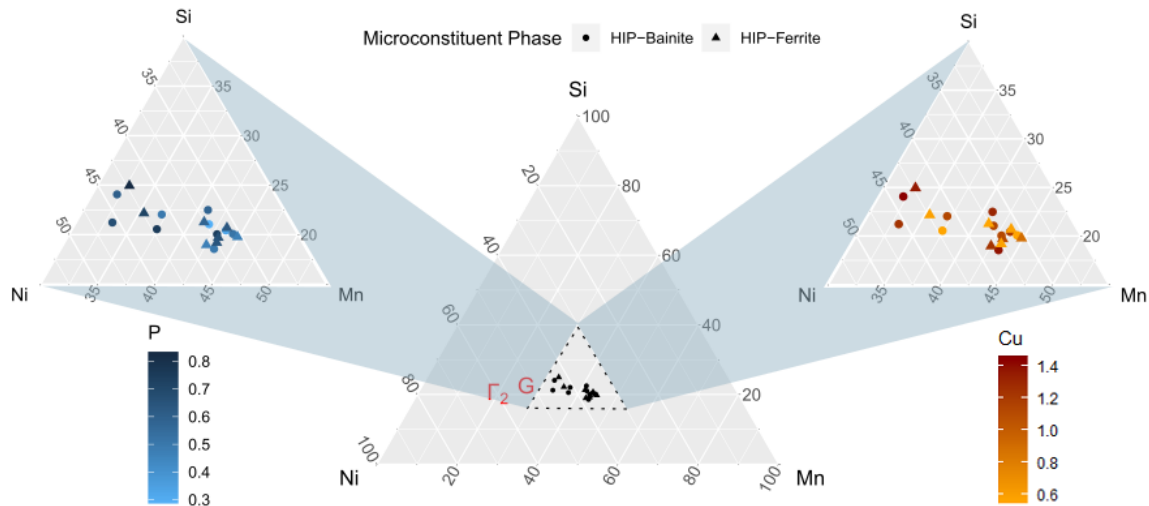


Figure 11: Ternary diagrams showing the average cluster compositions within APT samples taken from HIPed ferrite and bainite grains. The compositions of the proposed G and Γ_2 phases are denoted in red. The close-up ternary regions indicate the P (left) and Cu (right) concentrations.

bainitic samples is shown to coincide with a reduced Mn content within the tip, as illustrated in Figure 10. In this plot, Mn content is shown relative to the tip Ni content, as Ni concentration across the tips remain relatively constant (approximately that of the nominal alloy Ni composition), whereas Mn varies such as to be either higher or lower than the Ni content. The observed greater Mn variation in bainite is likely a result of the reduction in Mn within certain APT samples that were extracted in the vicinity of carbides. The irregular, lathed sub-structure of bainite increases the possibility of sampling from regions near a carbide compared to the more homogeneous ferrite grains.

Figure 11 shows the average cluster compositions obtained from the APT samples. The spread in compositions is limited, with no discernible trend in composition based on sample origin within the HIP steel microstructure. Of note is that these compositions fall near the proposed 'G' and ' Γ_2 ' phases ($\text{Ni}_{16}\text{Mn}_8\text{Si}_7$ and Ni_3MnSi respectively). The Cu and P cluster compositions are shown, due to them often being of interest in RPV steel clustering. However, it is clear from Figure 11 that there is no obvious compositional influence of these two elements with regards to the Mn:Si:Ni ratio of clusters in this case.

Nanohardness of the as-received HIPed SA508 showed the bainite and ferrite phases hardening of 1.94 ± 0.57 and 2.53 ± 0.63 respectively. The relative changes with respect to the as-received hardness are 0.53 for bainite and 0.79 for ferrite. The error bars are large both in the nanohardness data and clusters data from APT so firm conclusions cannot be derived on the behaviour of the two microstructures.

If a dispersed barrier hardening (DBH) model was applied to explain hardening induced by clustering it would, however, be found that bainite should have hardened more since the average diameter of the clusters observed in the bainite and ferrite by APT was 0.98nm for the ferrite and 1nm for bainite, and the cluster number density was also slightly higher in the bainite phase. In a DBH model of the type:

$$\Delta\sigma = \alpha \times M \times \mu \times b \times \sqrt{Nd} \quad [2]$$

where α is the obstacle strength and is considered to be from 0.1 to 0.3 for copper rich precipitates and from 0.05 to 0.1 for matrix features in RPV steels [46]. M is the Taylor factor and is considered equal to 3.06 for both *bcc* and *fcc* lattices, μ is the shear modulus (80GPa for ferritic steel) and b is the Burgers vector length (0.2485nm in *bcc* ferrite). N and d are the number density and the diameter of the features. To correlate the results from APT and nanohardness, there are two possibilities. Either the alpha factor is considered to be different for the two microstructures, with the obstacle strength being larger in the ferrite phase ($\alpha_{\text{ferrite}} > \alpha_{\text{bainite}}$) as if the clusters induce a stronger obstacle to dislocation motion. Or the increased hardening observed in the ferrite is due to the presence of additional sources of hardening beyond cluster formation.

The latter suggestion is an example of strengthening super-position [47] and can be applied to a combination of relatively weak obstacles induced by irradiation, such as dislocation loops and voids, or to pre-existing strong obstacles which contribute different amounts to the change in yield stress based on their distribution within the different grain types. Unfortunately, given the difficulties encountered in detecting radiation damage with TEM due to the presence of surface oxide, which produced black dots contrast, it was not possible to detect any other source of radiation damage at this stage, therefore applying the root-sum-square (RSS) model [48] to calculate the impact of multiple weak obstacles is not possible here. However, in this work it is strong dispersed obstacles ($\alpha > 0.6$) in the alloy, which are more likely to have influenced the difference in hardening experienced by ferrite and bainite. Here, strong obstacles likely take the form of carbides (and the intermetallics observed with STEM-EDX), which interact with the fine-scale weaker MNS clusters induced by neutron irradiation (either by acting as nucleation sites or changing the scale of the barrier-hardening region), altering the resultant dislocation-obstacle interactions and thus impacting the observed change in yield stress according to a linear sum (LS) model [47]. Thus, any difference in carbide densities between microconstituents could influence the change in yield stress, making the hardening dependent on the unirradiated material. The two possibilities (differing α values for clusters in ferrite and bainite, and the role of super-positioned hardening features) need to be further assessed.

Of importance when considering all of these results in the context of conventional RPV studies is to account for the lower irradiation temperature utilised as a consequence of the OPAL reactor set-up. Whilst it is still of interest to identify any influence of original microstructure on radiation response, as is the focus of this research, caution must be used when comparing cluster densities and compositions to those findings from experiments conducted at typical RPV operational temperature. The irradiation temperature of 155°C is likely to have impacted the cluster formation kinetics, density and compositions significantly, as a consequence of more stable point defects, as shown in previous low-temperature studies [46], [49], [50].

Summary and Conclusions

In this work novel HIPed SA508 Grade 3 steel was successfully subjected to neutron irradiation with the aim of investigating its viability for use in novel nuclear applications. This is the first instance in which material of this type has been analysed with respect to its neutron irradiation response. Focus was paid to the role of polygonal ferrite within the HIP microstructure in comparison to the bainite packets. The primary findings are as follows:

- APT did not show significant difference in radiation induced clustering of Mn-Ni-Si aggregates for bainite and ferrite samples taken from HIP SA508 steel irradiated to $\sim 100\text{mdpa}$ at 155°C .
- A slightly higher proportion of clustering solute (Mn, Ni, Si, P) was present within ferrite samples, but this did not correlate to an increase in the degree of clustering observed.
- Reduction in available solute, for bainitic clustering, may be a result of reduced Mn levels on account of increased likelihood of carbide proximity in this phase.
- Nanoindentation measurements showed that the two phases reached a similar hardness after neutron irradiation: the hardness of the bainite phase was $5.58 \pm 0.35\text{GPa}$ while the hardness of the ferrite phase was $5.71 \pm 0.43\text{GPa}$. However, as ferrite started as the softer phase, this hardened more than the bainite ($\Delta H = 2.53 \pm 0.63\text{GPa}$ for ferrite and $1.94 \pm 0.57\text{GPa}$ for bainite).
- TEM characterisation was not able to detect defects in the ferrite or bainite since black spots on the surface were identified as surface oxide.
- The use of the OPAL reactor at ANSTO as a method for the irradiation of nuclear materials has proven successful. There now exists the potential for further research utilising this protocol.
- In future research it may be worth examining the role of point defects and dislocations, both those existing as a result of the manufacturing process and those induced during irradiation, in the development of Mn-Ni-Si clusters. If the number of point defects and solute sinks is fixed post-irradiation, ferritic samples may approach a defined cluster number limit as fluence increases, whereas observing this limit in bainite may be less likely due to the number of existing nucleation sites in bainite being significantly higher prior to irradiation.

Acknowledgements

This work was financially supported by the UK Engineering and Physical Sciences Research Council (EPSRC) through the grants EP/P005101/1, EP/P005640/1 and EP/P003591/1.

The research used UKAEA's Materials Research Facility, which has been funded by, and is part of, the UK's National Nuclear User Facility and the Henry Royce Institute for Advanced Materials.

The APT facilities at the University of Oxford are funded by the EPSRC (EP/M022803/1).

The authors would also like to thank Rolls Royce Plc for supplying the material studied in this work, John Claridge at the MRF for his help in preparing the samples for FIB and nanoindentation, and Dr B.M Jenkins for use of his cluster analysis R code.

References

- [1] H. V. Atkinson and S. Davies, "Fundamental aspects of hot isostatic pressing: An overview," *Metall. Mater. Trans. A Phys. Metall. Mater. Sci.*, vol. 31, no. 12, pp. 2981–3000, Dec. 2000.
- [2] X. Lou and D. Gandy, "Advanced Manufacturing for Nuclear Energy," *JOM*, vol. 71, no. 8, pp. 2834–2836, Aug. 2019.
- [3] S. Irukuvarhula, H. Hassanin, C. Cayron, M. M. Attallah, D. Stewart, and M. Preuss, "Evolution of grain boundary network topology in 316L austenitic stainless steel during powder hot isostatic pressing," *Acta Mater.*, vol. 133, pp. 269–281, 2017.
- [4] O. K. Chopra and A. S. Rao, "Degradation of LWR core internal materials due to neutron irradiation," *NUREG/CR-7027 ANL-10/11 Report, Environ. Sci. Div. Argonne Natl. Lab*, no. January, 2010.
- [5] E. A. Marquis, "Atom probe tomography applied to the analysis of irradiated

- microstructures," *J. Mater. Res.*, vol. 30, no. 09, pp. 1222–1230, May 2015.
- [6] M. K. Miller and P. Pareige, "Atomic Level Characterization of Neutron Irradiated Pressure Vessel Steels," in *Materials Research Society Symposium Proceedings*, 2001, vol. 650, p. R6.1.1-12.
 - [7] G. R. Odette, "On the dominant mechanism of irradiation embrittlement of reactor pressure vessel steels," *Scr. Metall.*, vol. 17, no. 10, pp. 1183–1188, Oct. 1983.
 - [8] G. R. Odette, C. L. Liu, and B. D. Wirth, "On the composition and structure of nanoprecipitates in irradiated pressure vessel steels," in *Materials Research Society Symposium - Proceedings*, 1997, vol. 439, pp. 457–469.
 - [9] G. R. Odette, "Radiation Induced Microstructural Evolution in Reactor Pressure Vessel Steels," *MRS Proc.*, vol. 373, p. 137, 1995.
 - [10] P. B. Wells, "The Character, Stability and Consequences of Mn-Ni-Si Precipitates in Irradiated Reactor Pressure Vessel Steels," UCSB, 2016.
 - [11] P. B. Wells *et al.*, "Evolution of manganese-nickel-silicon-dominated phases in highly irradiated reactor pressure vessel steels," *Acta Mater.*, vol. 80, pp. 205–219, Nov. 2014.
 - [12] M. K. Miller, K. A. Powers, R. K. Nanstad, and P. Efsing, "Atom probe tomography characterizations of high nickel, low copper surveillance RPV welds irradiated to high fluences," *J. Nucl. Mater.*, vol. 437, no. 1–3, pp. 107–115, 2013.
 - [13] P. D. Edmondson, C. M. Parish, and R. K. Nanstad, "Using complimentary microscopy methods to examine Ni-Mn-Si-precipitates in highly-irradiated reactor pressure vessel steels," *Acta Mater.*, vol. 134, pp. 31–39, Aug. 2017.
 - [14] B. M. Jenkins *et al.*, "The Effect of Composition Variations on the Response of Steels Subjected to High Fluence Neutron Irradiation," *Materialia*, p. 100717, May 2020.
 - [15] M. K. Miller and K. F. Russell, "Embrittlement of RPV steels: An atom probe tomography perspective," *J. Nucl. Mater.*, vol. 371, no. 1–3, pp. 145–160, 2007.
 - [16] N. Almirall *et al.*, "On the elevated temperature thermal stability of nanoscale Mn-Ni-Si precipitates formed at lower temperature in highly irradiated reactor pressure vessel steels," *Sci. Rep.*, vol. 9, no. 1, pp. 1–12, Jul. 2019.
 - [17] G. R. Odette, N. Almirall, P. B. Wells, and T. Yamamoto, "Precipitation in reactor pressure vessel steels under ion and neutron irradiation: On the role of segregated network dislocations," *Acta Mater.*, vol. 212, p. 116922, Jun. 2021.
 - [18] J. R. Hawthorne, "Composition influences and interactions in radiation sensitivity of reactor vessel steels," *Nucl. Eng. Des.*, vol. 89, no. 1, pp. 223–232, Nov. 1985.
 - [19] M. M. Ghoneim and F. H. Hammad, "Pressure vessel steels: Influence of chemical composition on irradiation sensitivity," *Int. J. Press. Vessel. Pip.*, vol. 74, no. 3, pp. 189–198, Dec. 1997.
 - [20] M. G. Burke, R. J. Stofanak, J. M. Hyde, C. A. English, and W. L. Server, "Microstructural aspects of irradiation damage in A508 Gr 4N forging steel: Composition and flux effects," 2004.
 - [21] N. Almirall, P. B. Wells, T. Yamamoto, K. Yabuuchi, A. Kimura, and G. R. Odette, "On the use of charged particles to characterize precipitation in irradiated reactor pressure vessel steels with a wide range of compositions," *J. Nucl. Mater.*, vol. 536, p. 152173, Aug. 2020.

- [22] B. Marini, X. Averty, P. Wident, P. Forget, and F. Barcelo, "Effect of the bainitic and martensitic microstructures on the hardening and embrittlement under neutron irradiation of a reactor pressure vessel steel," *J. Nucl. Mater.*, vol. 465, pp. 20–27, Oct. 2015.
- [23] S. J. Zinkle and G. S. Was, "Materials challenges in nuclear energy," *Acta Mater.*, vol. 61, no. 3, pp. 735–758, 2013.
- [24] K. T. Park, S. W. Hwang, J. H. Ji, and C. H. Lee, "Inclusions nucleating intragranular polygonal ferrite and acicular ferrite in low alloyed carbon manganese steel welds," *Met. Mater. Int.*, vol. 17, no. 2, pp. 349–356, 2011.
- [25] S. G. Druce, G. Gage, and G. Jordan, "Effect of ageing on properties of pressure vessel steels," *Acta Metall.*, vol. 34, no. 4, pp. 641–652, Apr. 1986.
- [26] C. Gasparrini *et al.*, "Micromechanical testing of unirradiated and helium ion irradiated SA508 reactor pressure vessel steels: Nanoindentation vs in-situ microtensile testing," *Mater. Sci. Eng. A*, vol. 796, p. 139942, Oct. 2020.
- [27] D. Legland, I. Arganda-Carreras, and A. P., "MorphoLibJ: integrated library and plugins for mathematical morphology with ImageJ," *Bioinformatics*, vol. 32, no. 22, pp. 3532–3534, 2016.
- [28] R. E. Reed-Hill and R. Abbaschian, "The Bainite Reaction," in *Physical Metallurgy Principles*, 3rd ed., PWS Publishing, 1994.
- [29] ANSTO, "OPAL Research Reactor Safety Analysis Report: Chapter 11." [Online]. Available: <https://www.arpansa.gov.au/sites/default/files/legacy/pubs/regulatory/opal/op/SAR/ch11.pdf>.
- [30] A. Aitkaliyeva, J. W. Madden, B. D. Miller, J. I. Cole, and J. Gan, "Comparison of preparation techniques for nuclear materials for transmission electron microscopy (TEM)," *J. Nucl. Mater.*, vol. 459, pp. 241–246, 2015.
- [31] M. K. Miller, K. F. Russell, and G. B. Thompson, "Strategies for fabricating atom probe specimens with a dual beam FIB," *Ultramicroscopy*, vol. 102, no. 4, pp. 287–298, 2005.
- [32] L. T. Stephenson, M. P. Moody, P. V. Liddicoat, and S. P. Ringer, "New techniques for the analysis of fine-scaled clustering phenomena within Atom Probe Tomography (APT) data," in *Microscopy and Microanalysis*, 2007, vol. 13, no. 6, pp. 448–463.
- [33] J. M. Hyde *et al.*, "Analysis of Radiation Damage in Light Water Reactors: Comparison of Cluster Analysis Methods for the Analysis of Atom Probe Data," *Microsc. Microanal.*, vol. 23, no. 02, pp. 366–375, Apr. 2017.
- [34] J. M. Hyde, A. Cerezo, and T. J. Williams, "Statistical analysis of atom probe data: Detecting the early stages of solute clustering and/or co-segregation," *Ultramicroscopy*, vol. 109, no. 5, pp. 502–509, Apr. 2009.
- [35] J. M. Hyde, E. A. Marquis, K. B. Wilford, and T. J. Williams, "A sensitivity analysis of the maximum separation method for the characterisation of solute clusters," *Ultramicroscopy*, vol. 111, pp. 440–447, 2011.
- [36] M. K. Miller, K. F. Russell, M. A. Sokolov, and R. K. Nanstad, "APT characterization of irradiated high nickel RPV steels," *J. Nucl. Mater.*, vol. 361, no. 2-3 SPEC. ISS., pp. 248–261, 2007.
- [37] J. M. Hyde and C. A. English, "An Analysis of the Structure of Irradiation Induced Cu-Enriched Clusters in Low and High Nickel Welds," in *Materials Research Society Symposium Proceedings*, 2000, vol. 650, p. R6.6.

- [38] P. D. Styman, J. M. Hyde, K. Wilford, and G. D. W. Smith, "Quantitative methods for the APT analysis of thermally aged RPV steels," *Ultramicroscopy*, vol. 132, pp. 258–264, Sep. 2013.
- [39] S. Shu, N. Almirall, P. B. Wells, T. Yamamoto, G. R. Odette, and D. D. Morgan, "Precipitation in Fe-Cu and Fe-Cu-Mn model alloys under irradiation: Dose rate effects," *Acta Mater.*, vol. 157, pp. 72–82, Sep. 2018.
- [40] F. Vurpillot, A. Bostel, and D. Blavette, "Trajectory overlaps and local magnification in three-dimensional atom probe," *Appl. Phys. Lett.*, vol. 76, no. 21, pp. 3127–3129, May 2000.
- [41] H. Ke *et al.*, "Thermodynamic and kinetic modeling of Mn-Ni-Si precipitates in low-Cu reactor pressure vessel steels," *Acta Mater.*, vol. 138, pp. 10–26, 2017.
- [42] J. H. Ke, H. Ke, G. R. Odette, and D. Morgan, "Cluster dynamics modeling of Mn-Ni-Si precipitates in ferritic-martensitic steel under irradiation," *J. Nucl. Mater.*, vol. 498, pp. 83–88, Jan. 2018.
- [43] E. Meslin, B. Radiguet, and M. Loyer-Prost, "Radiation-induced precipitation in a ferritic model alloy: An experimental and theoretical study," *Acta Mater.*, vol. 61, pp. 6246–6254, Sep. 2013.
- [44] N. Almirall *et al.*, "Precipitation and hardening in irradiated low alloy steels with a wide range of Ni and Mn compositions," *Acta Mater.*, vol. 179, pp. 119–128, Oct. 2019.
- [45] T. R. Allen *et al.*, "Characterization of microstructure and property evolution in advanced cladding and duct: Materials exposed to high dose and elevated temperature," *J. Mater. Res.*, vol. 30, no. 09, pp. 1246–1274, 2015.
- [46] E. D. Eason, G. R. Odette, R. K. Nanstad, and T. Yamamoto, "A physically-based correlation of irradiation-induced transition temperature shifts for RPV steels," *J. Nucl. Mater.*, vol. 433, no. 1–3, pp. 240–254, 2013.
- [47] G. R. Odette and G. E. Lucas, "Recent progress in understanding reactor pressure vessel steel embrittlement," *Radiat. Eff. Defects Solids*, vol. 144, no. 1–4, pp. 189–231, Jun. 1998.
- [48] A. J. E. Foreman and M. J. Makin, "Dislocation movement through random arrays of obstacles," *Can. J. Phys.*, vol. 45, no. 2, pp. 511–517, Feb. 1967.
- [49] R. J. McElroy, T. J. Williams, F. M. D. Boydon, and B. Hemsworth, "Low temperature embrittlement of LWR RPV support structures," *Int. J. Press. Vessel. Pip.*, vol. 54, no. 1–2, pp. 171–211, Jan. 1993.
- [50] K. Dohi, T. Onchi, F. Kano, K. Fukuya, M. Narui, and H. Kayano, "Effect of neutron flux on low temperature irradiation embrittlement of reactor pressure vessel steel," *J. Nucl. Mater.*, vol. 265, no. 1–2, pp. 78–90, Feb. 1999.